Journal of Power Sources 183 (2008) 660–667

Contents lists available at ScienceDirect

Journal of Power Sources

journal homepage: www.elsevier.com/locate/jpowsour

Investigation of iron–chromium–niobium–titanium ferritic stainless steel for solid oxide fuel cell interconnect applications

Zhenguo Yang*, Guan-Guang Xia, Chong-Min Wang, Zimin Nie, Joshua Templeton, Jeffry W. Stevenson, Prabhakar Singh

Pacific Northwest National Laboratory, 902 Battelle, Blvd, Richland, WA 99352, United States

ARTICLE INFO

Article history:
Received 29 April 2008
Accepted 2 May 2008
Available online 21 May 2008

Keywords:
Solid oxide fuel cell
Interconnect
Oxidation
Coating

ABSTRACT

As part of an effort to develop cost-effective ferritic stainless steel-based interconnects for solid oxide fuel cell (SOFC) stacks, both bare AISI441 and AISI441 coated with $(Mn,Co)_3O_4$ protection layers were studied in terms of its metallurgical characteristics, oxidation behavior, and electrical performance. The addition of minor alloying elements, in particular Nb, led to formation of Laves phases both inside grains and along grain boundaries. In particular, the Laves phase which precipitated out along grain boundaries during exposure at intermediate SOFC operating temperatures was found to be rich in both Nb and Si. The capture of Si in the Laves phase minimized the Si activity in the alloy matrix and prevented formation of an insulating silica layer at the scale/metal interface, resulting in a reduction in area-specific electrical resistance (ASR). However, the relatively high oxidation rate of the steel, which leads to increasing ASR over time, and the need to prevent volatilization of chromium from the steel necessitates the application of a conductive protection layer on the steel. In particular, the application of a $Mn_{1.5}Co_{1.5}O_4$ spinel protection layer substantially improved the electrical performance of the 441 by reducing the oxidation rate.

1. Introduction

Oxidation resistant alloys, in particular ferritic stainless steels, are considered to be promising candidate materials for interconnect applications in SOFC stacks operating in the intermediate temperature range of 650–800 °C [1–5]. One issue associated with the use of steels in this application, however, is the high electrical resistance that arises from the growth of an oxide scale on the alloys during high temperature exposure. In addition to the scale (chromia or other semi-conductive oxides such as spinels), an insulating silica layer often forms at the scale/metal interface due to the presence of residual Si in the alloy. This silica layer, if continuous, can drastically increase the electrical resistance of metallic interconnects. For example, with <1% residual Si, AISI430 (17% Cr) often forms a silica sub-layer at the scale/metal interface under SOFC operating conditions, increasing the combined steel/scale electrical resistance [5–7]. To improve the scale conductivity, several alloys, including Crofer 22 APU [8–10] and ZMG232 [11,12], have been specifically developed in the past few years for the SOFC interconnect application. These alloys contain a small amount of Mn that results in formation of a conductive dual layer scale consisting of a $(Mn,Cr)_3O_4$ top layer and chromia sub-layer. Also, to control residual elements such as Si and mitigate their negative effects for the interconnect applications, additional processing such as vacuum refining is commonly used. Overall, these newly developed alloys demonstrate improved suitability for the interconnect application, due in part to their improved electrical performance. However, the vacuum refining significantly adds to the material cost, thereby partially offsetting the anticipated cost reduction associated with the replacement of ceramic interconnects with alloy-based interconnects.

Alternatively, modification of the alloy chemistry can potentially be used to avoid silica layer formation without the need for expensive vacuum refining steps. The alloying approach can be traced back to a study by Dulieu et al. [6] that evaluated conventional grade (i.e., alloys prepared via a conventional melting approach, without extra refining) ferritic stainless steels 1.4510 (17% Cr–Ti, equivalent to AISI439) and 1.4509 (18% Cr–Nb–Ti, AISI441), in comparison with 1.4016 (17% Cr, AISI430). Unlike 1.4016, the former two ferritic stainless steels did not exhibit formation of a silica sub-layer at the scale/metal interfaces, in spite of the presence of over 0.5% residual Si in the Fe–Cr substrates. Consequently these two ferritic stainless steels demonstrated a lower area-specific electrical resistance (ASR) than 1.4016. Also the minor alloy additions appeared to alter the oxidation behavior by promoting formation of a chromia scale. Since then, several other ferritic stainless steels with minor

* Corresponding author. Tel.: +1 509 375 3756; fax: +1 509 375 2186.
E-mail address: Zgary.yang@pnl.gov (Z. Yang).

0378-7753/$ – see front matter © 2008 Elsevier B.V. All rights reserved.
doi:10.1016/j.jpowsour.2008.05.037

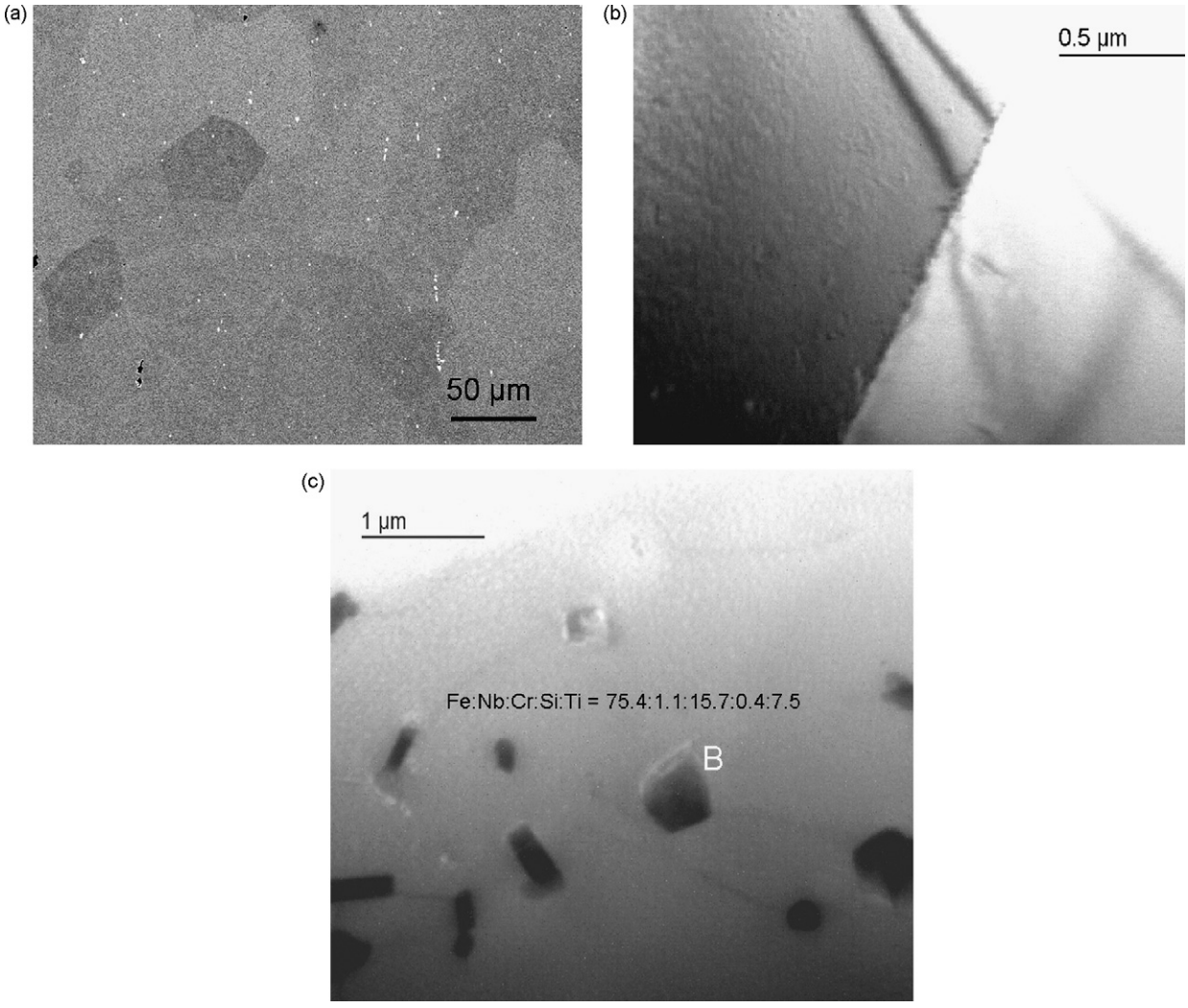

Fig. 1. Microstructures of as-received 441: (a) an SEM image; (b) a TEM bright field image of a grain boundary, and (c) a TEM bright field image of second phase precipitates and EDS analysis.

additions of Nb, Ti, and/or other Laves phase formation elements such as W, Mo, etc., have been developed or evaluated. In addition to improved electrical performance, the Fe–Cr–Nb(–Mo–W–)–Ti ferritic stainless steels were also reported to exhibit improved mechanical strength due to the Laves phase formation [7,13–15].

To gain further insight into the effects of minor alloying additions, the metallurgical characteristics, oxidation behavior and electrical performance of AISI411, a commercial ferritic stainless steel were investigated. In addition, potential benefits of protective spinel coatings were examined by applying protective layers of $(Mn,Co)_3O_4$ spinel to 441, and comparing the behavior of coated 441 to that of uncoated 441. By restricting oxygen inward diffusion, and chromium outward diffusion, the spinel coatings have been found to be effective in reducing chromium volatility, and in improving both surface stability and electrical stability [16–22]. This paper reports the results of the study, and discusses the suitability of the steel for SOFC interconnect applications.

Table 1
Yield strength ($Rp_{0.2}$) of ferritic stainless steels [26,34]

Temperatures		0.2% Off set yield strength (MPa)	
Fahrenheit (F)	Celsius (°C)	T441	Crofer22 APU
77	25	302	275
400	204	251	167
800	427	224	145
1200	649	171	60
1400	760	83	31

2. Experimental

2.1. Sample preparation

The ferritic stainless steel studied was AISI441, a commercial product of Allegheny Ludlum Inc., with a chemical composition of 17.6% (weight) Cr, 0.33% Mn, 0.47% Si, 0.46% Nb, 0.18% Ti, 0.20% Ni, 0.01% C, 0.045% Al, 0.024% P, 0.001% S, balance Fe. The steel plate, with a thickness of 1.5 mm, was cut into 25.4 mm × 12.7 mm coupons, and cleaned in an ultrasonic acetone bath for 5 min and then rinsed in alcohol prior to testing or application of the spinel coating. A slurry-based approach [20] was used to apply the $Mn_{1.5}Co_{1.5}O_4$ spinel protection layers on the steel coupons. After coating application, the dried coupons were first heat-treated in a reducing environment (2.75% H_2 + 3% H_2O + 94.25% Ar) for 2 h and then oxidized in ambient air at 800 °C for 1 h.

2.2. Oxidation kinetics measurements

Bare and coated steel coupons were evaluated via isothermal oxidation tests in ambient air. The isothermal oxidation testing in air was performed by suspending the bare or coated coupons from an alumina rod in a tube furnace. The coupons were heated to 800 °C at 5 °C min^{-1}, held at this temperature for 100–1200 h, and then cooled to room temperature. A steady flow of ambient air (w/1–2% water) was provided throughout the oxidation tests. The oxidized coupons were then weighed prior to structural and microstructural characterization.

2.3. Electrical resistance measurements

The electrical resistance of bare and coated 441 was measured using a four-probe DC technique. Details of the test arrangement were reported in a previous publication [16]. $La_{0.8}Sr_{0.2}MnO_3$ (LSM) contact paste was applied between two identical coupons and Pt wires were spot-welded to the coupons. During the test, a constant current density of 500 mA cm^{-2} was applied to the coupons through two Pt leads, while the voltage drop across the two alloy coupons was measured with the other two Pt leads. The area specific resistance (ASR, expressed in ohm cm^2) of the scales were then calculated according to Ohm's Law, ASR = $V/2i$, where V is the voltage drop and i is the current density. The factor of 2 was included to account for the fact that the voltage drop was measured across two oxide scales connected in series.

2.4. XRD, SEM, and TEM analyses

XRD analysis on the oxidized alloy coupons was performed using a Philips XRG-3100 X-ray Generator with Cu Kα radiation. SEM analysis was performed using a JEOL scanning electron microscope (model 5900 LV) equipped with energy-dispersive spectroscopic (EDS) capability at an operating voltage of 20 kV. After SEM analysis of the surface, the coupons were epoxy-mounted, sectioned, polished, and further examined by SEM. In addition, high resolution transmission electron microscopy (HRTEM) equipped with an EDS analytical system was also used to study the steel samples. A thin foil cross section for the TEM analysis was prepared by standard tripod wedge polishing, followed by Ar-ion beam thinning for electron transparency. The JEOL TEM 2010 microscope was operated on a voltage of 200 kV, with a specified point-to-point resolution of 0.194 nm. Composition of the precipitates in the steel substrate was analyzed using the EDS with an energy resolution of 136 eV (Oxford link EDS spectrometer running ISIS). Due to the thinness of the specimen, the absorption effect was ignored during the quantification for the spectra.

3. Results and discussion

3.1. Metallurgy of Ferritic stainless steel AISI T441

Fig. 1(a) shows an SEM back-scattering image of the microstructure of the as-received 441. Due to the different contrast resulting

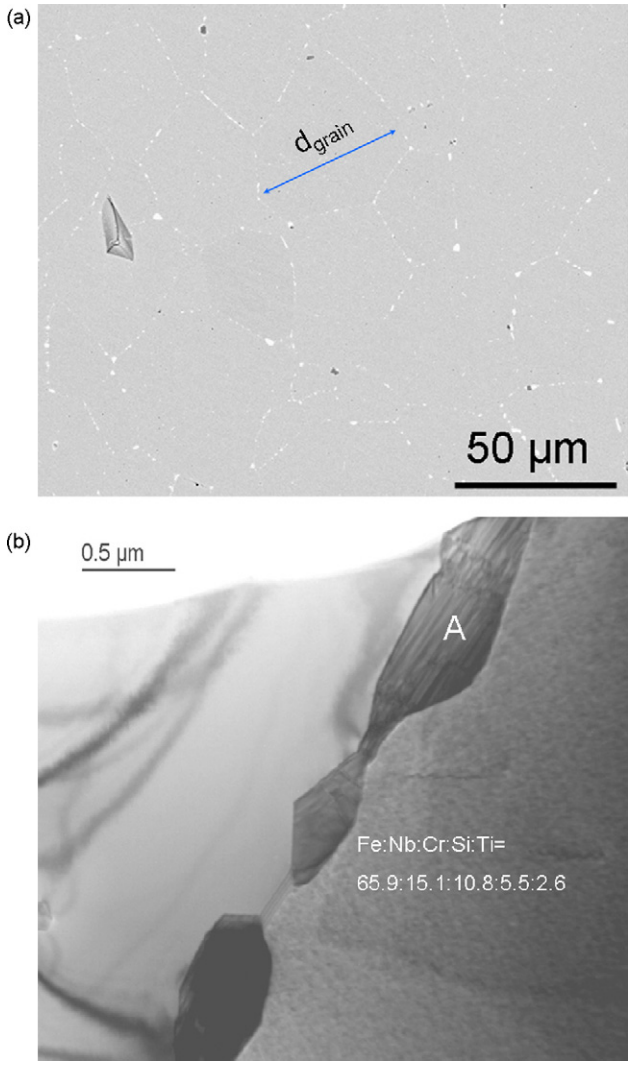

Fig. 2. Microstructures of 441 after oxidation in air for 300 h at 800 °C and cooling to room temperature via static air cooling: (a) an SEM image and (b) a TEM bright field image.

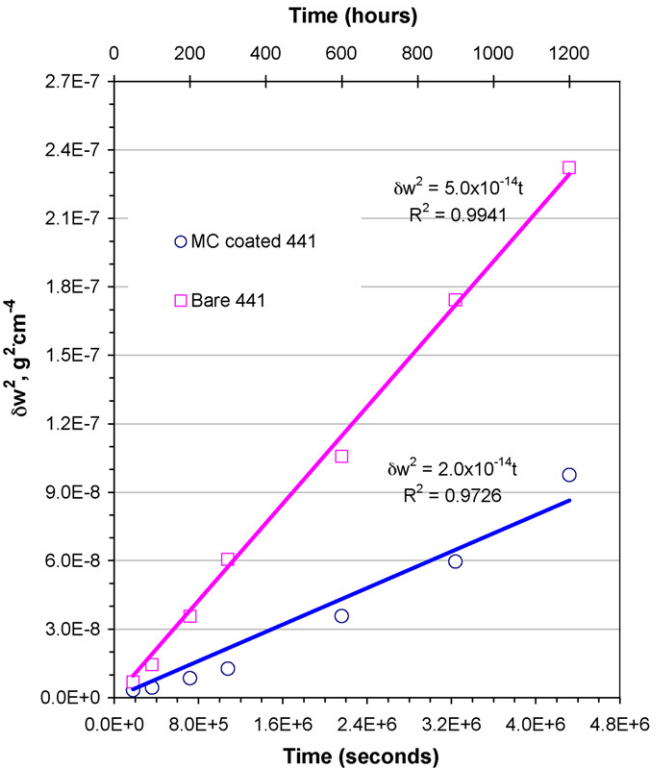

Fig. 3. Weight gain (w^2, g^2 cm^{-4}) of bare and spinel-coated 441 as a function of time during oxidation in air at 800 °C.

from different crystal orientation, it is apparent that the grains ranged in size from around 20–60 μm. Second phases (white in appearance) were observed to be randomly distributed within the grains. SEM/EDS point analysis indicated that the second phases were rich in Nb and Ti, but contained little, if any, Si. This was further confirmed by TEM observation and EDS analysis, as shown in Fig. 2(b). The point TEM/EDS point analysis at the precipitate "B" found 75.4 Fe, 1.1 Nb, 15.7 Cr, 0.4 Si, 7.5 Ti (atomic%). Also the TEM analyses revealed clean grain boundaries with no apparent second phase precipitation, as shown in Fig. 3(c). The intra-grain precipitates appeared to be a Laves phase of $MgZn_2$ crystal structure, although carbides and nitrides of Nb and Ti are thermodynamically possible as well [23,24]. It was previously documented that Nb-additions can result in $NbFe_2$ Laves phase formation in Fe–Cr–Nb base alloy substrates [25,26]. Nb-base Laves phases involving other elements, such as W, Mo, Cr, Si, Ti, etc., were also reported to be thermodynamically favorable [27–30].

After oxidation in air at elevated temperature, second phases were observed at the grain boundaries. Fig. 2(a) shows the SEM back-scattering image of a sample after oxidation in air at 800 °C for 300 h. The precipitates along grain-boundaries delineate the grain sizes, which appear to be similar to that of the as-received material, indicating little change in grain size during the oxidation. It appears that the precipitates may act to stabilize the grain boundaries, avoiding grain growth at the tested temperatures. TEM analyses, as shown in Fig. 2(b), further confirmed the presence of second phases that precipitated out along grain boundaries in the oxidized samples. Further EDS point analysis on a precipitate, marked as "A", indicated 65.9 Fe, 15.1 Nb, 10.8 Cr, 5.5 Si, 2.6 Ti. The precipitates along grain boundaries were rich in both Nb and Si, in contrast to the intra-grain precipitates that contained little, if any, Si. Further micro-diffraction analysis on the precipitate confirmed that the second phase at the grain boundaries was a Laves phase. This is consistent with results reported previously [13–15] on Fe–Cr–Nb base ferritic stainless steels. These alloys also exhibit improved mechanical strength, in particular at high temperatures, due to the minor-alloy element additions. For example, T441 demonstrates a yield strength in the SOFC intermediate operating temperature range (650–800 °C) that is two to three times higher than ferritic stainless steel without minor additions of strengthening elements such as Nb (see Table 1). Similarly, Fe–Cr–Nb–W–Si was reported to have relatively high creep rupture strength at SOFC operating temperatures [14]. The improved mechanical strength and high temperature capability are mainly attributed to solid solution strengthening by Nb (as well as Mo and W) [31], and precipitation strengthening through formation of the Laves phase [14].

3.2. Oxidation of bare and coated 441

Fig. 3 shows the oxidation kinetics, in terms of weight gain as a function of time, of bare 441, along with that of 441 coated with the $Mn_{1.5}Co_{1.5}O_4$ spinel protection layer. The measurements were carried out in ambient air at 800 °C for up to 1200 h. For bare 441, the weight gain due to the scale growth on its surface approximately followed the classic parabolic relationship with time. The calculated rate constant (5.0×10^{-14} g^2 cm^{-4} s^{-1}) is com-

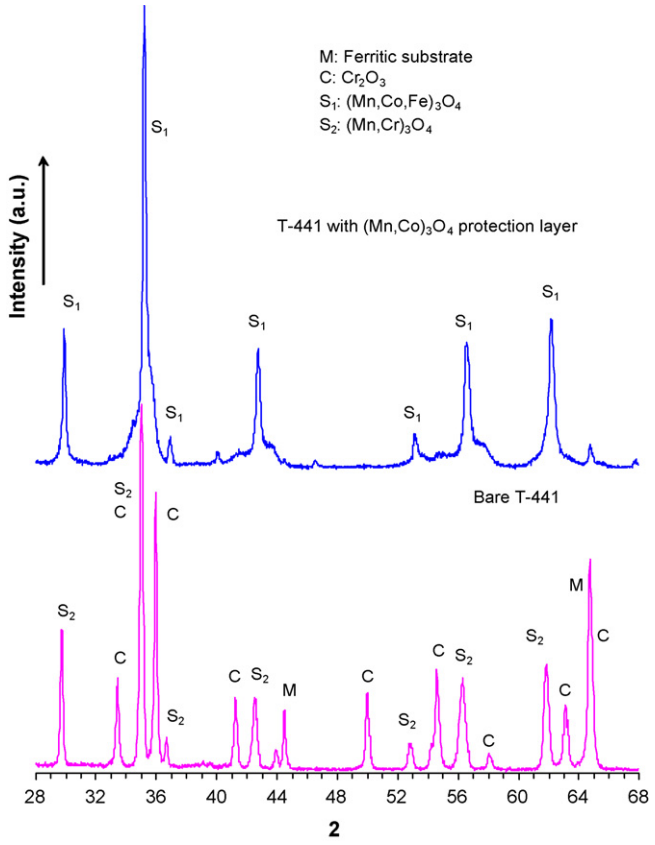

Fig. 4. XRD patterns of scales grown on bare and spinel-coated 441 during oxidation in air at 800 °C for 300 h.

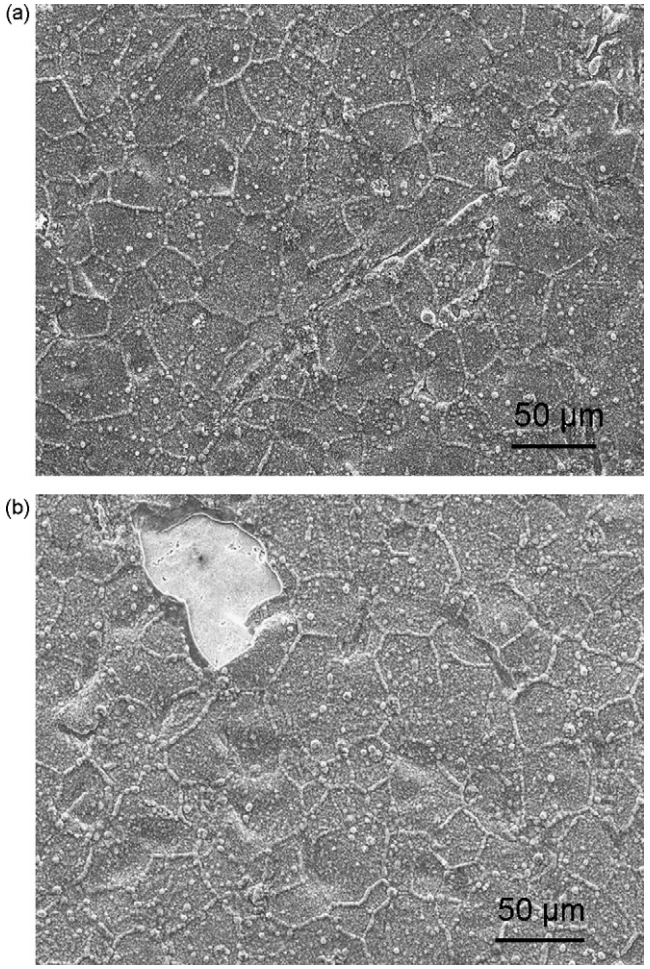

Fig. 5. SEM surface microstructures of 441 after oxidation at 800 °C in air for (a) 300 and (b) 900 h.

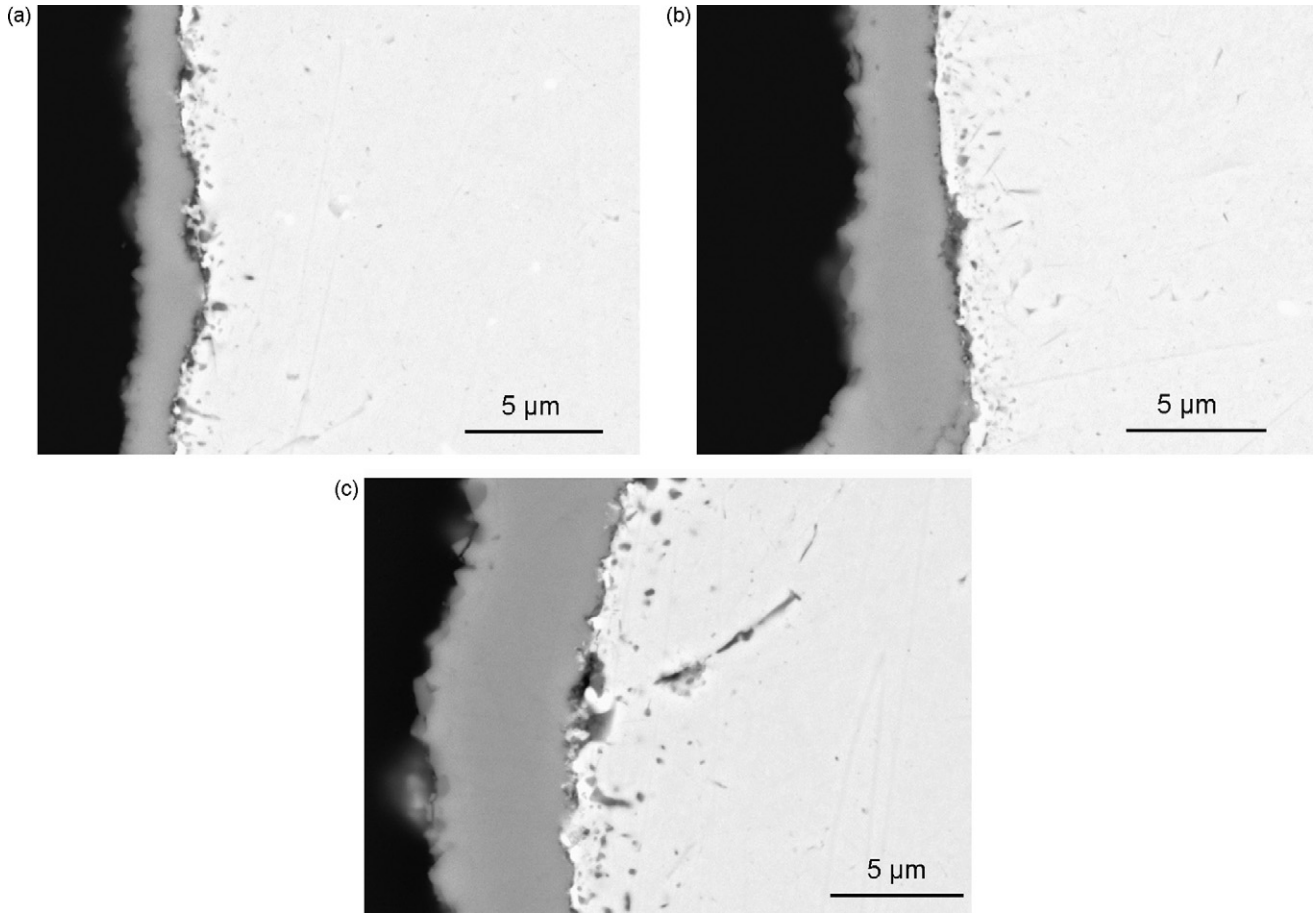

Fig. 6. SEM cross-sections of 441 after oxidation in air at 800 °C for (a) 100 h, (b) 300 h and (c) 900 h.

parable to that of Crofer 22 APU, and slightly lower than that of AISI430 under similar testing conditions [6,10]. The coated 441 exhibited lower weight gain with time under the identical testing conditions. Since the coatings appeared to be impermeable to air (i.e., with closed pore microstructure), the weight change of the coated samples is attributed to oxygen ion inward diffusion through the coating leading to subsequent scale growth beneath the coating [16]. The oxidation rate is, however, 2–3 times lower that of the bare alloy, indicating the effectiveness of the coating in reducing the scale growth rate beneath the spinel protection layers.

X-ray diffraction analysis, as shown in Fig. 4, indicated that the scale grown on bare 441 was comprised of chromia and a spinel phase, which was likely $(Mn,Cr)_3O_4$ considering the presence of residual Mn in the steel. Cross-section SEM/EDS analysis on the oxidized samples (similar to the analysis shown in Fig. 10a) confirmed that, as in the case of Crofer 22 APU, the scale grown on 441 was a dual layer structure with an Mn-rich spinel top layer and chromia-rich sub-layer [10]. In addition, SEM surface observation on the bare samples after oxidation, as shown in Fig. 5(a), found coarse $(Mn,Cr)_3O_4$ spinel crystallites dotting the grain boundaries of the surface scale. This indicates that, apparently, grain boundaries acted as fast diffusion paths for Mn and Cr. No spallation was observed in the early stages of oxidation, but after 900 h, localized spallation was observed, with the spallation edges coinciding with grain boundaries (Fig. 5b). The observation is consistent with recent publications that indicated a weak adherence of the scale [15,32]. Further SEM cross-section examination, as shown in Fig. 6, found uniform scale growth on the steel substrates, with the scale thickness, as expected, increasing with oxidation time. Occasional delamination observed at the scale/alloy interface may be an indication of weak adherence of the scale to the steel substrate.

Results of X-ray diffraction analysis of the coated samples are shown in Fig. 4, along with that of bare samples. Previous work [17] indicated a single cubic phase for $Mn_{1.5}Co_{1.5}O_4$ spinel at elevated temperatures (e.g., 800 °C), with tetragonal domains forming in the cubic matrix (through a diffusionless, martensitic transformation) during cooling to room temperature. That is, the high temperature cubic structure of the spinel would transform into a dual phase structure consisting of a cubic phase and a tetragonal phase. The present study found, however, a different structural behavior for the spinel coating on 441. After 300 h at 800 °C, a single cubic spinel phase was observed at room temperature, instead of the aforementioned dual cubic and tetragonal mixed structure. EDS analysis on cross-sections indicated the presence of Fe in the coating, so it is assumed that the diffusion of Fe from the alloy into the coating was responsible for the observed stabilization of the high temperature cubic structure. Formation of solid solution of $(Mn,Fe)_3O_4$ or $(Mn,Fe,Co)_3O_4$ was reported to be thermodynamically favorable [33]. Importantly, however, SEM/EDs analyses found no Cr penetration into the spinel coatings (as will be discussed in the next section). Thus, the spinel protection layers acted as an effective barrier to Cr-outward transport. SEM cross-section analyses, as shown in Fig. 7, indicated gas-tight (i.e., closed porosity) coatings. The

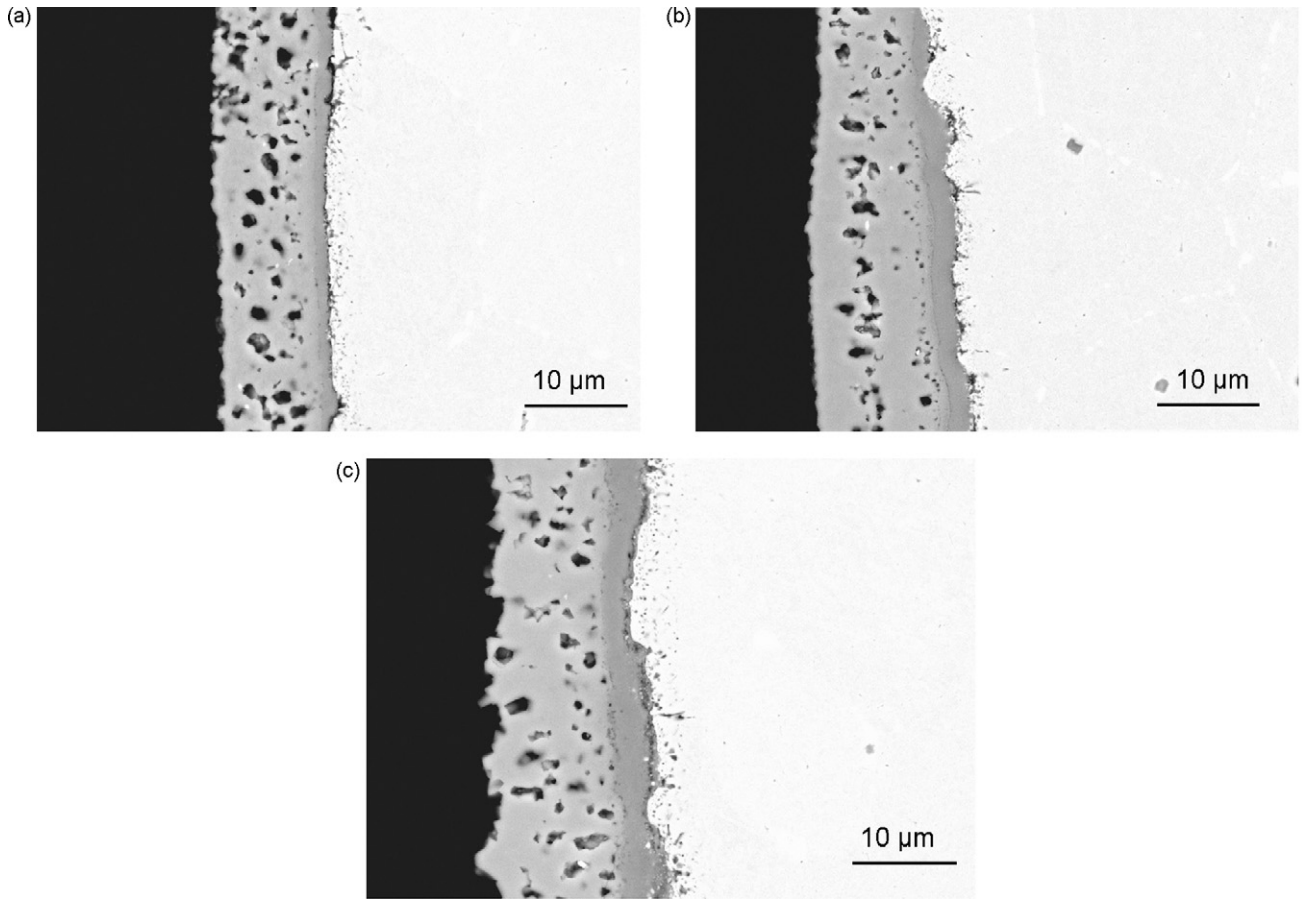

Fig. 7. SEM cross-sections of spinel-coated 441 after oxidation in air at 800 °C for (a) 100 h, (b) 300 h and (c) 900 h.

scales grown beneath the protection layers were distinguishable and their thickness increased with time. The coatings were apparently well-bonded to the substrates, as no spallation of coatings was observed.

Overall, it appears that 441 formed a scale that is similar to that grown on Crofer22 APU, which is comprised of a $(Mn,Cr)_3O_4$ top layer and a chromia or chromia-rich sub-layer. There were qualitative indications that the bonding of the scale to the steel substrate might be weaker than that observed for Crofer 22 APU, possibly due to the absence of rare earth elements in the 441. The steel's oxidation resistance or surface stability was improved by application of $Mn_{1.5}Co_{1.5}O_4$ spinel protection layers, whose room temperature structure evolved from a cubic/tetragonal mixture to a single cubic structure, due to Fe migration from the steel substrate into the coating.

3.3. Electrical performance

In addition to satisfactory structural and surface stability, candidate interconnect alloys must demonstrate a low electrical resistance as well, in order to minimize power loss. Fig. 8 shows the area specific resistance of bare 441 as a function of time, along with that of 441 with a $Mn_{1.5}Co_{1.5}O_4$ spinel protection layer or coating. The bare 441 exhibited an initially low ASR that increased steadily over time due to oxide scale growth, reaching about 20 mΩ cm^2 after 500 h. In comparison, the ASR of the coated 441 started at a slightly higher value than that of the bare 441, due to the relatively high contact resistance with the oxide coating compared to that with the bare metal. But the resistance with the coated 441 then decreased slowly over the span of the test, and ended up at about 13 mΩ cm^2 after 500 h of testing. Similarly, the resistance of bare 441 was measured at 750 °C and compared with that of a coated sample (see Fig. 9). The ASR of the bare 441 started at a relatively low value that increased over time, although, as expected, the rate of increase was lower than that at 800 °C due to a lower scale growth rate. The coated sample exhibited an ASR that again

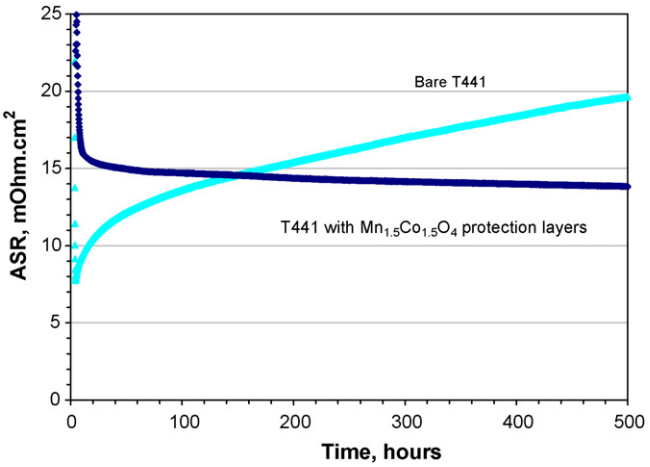

Fig. 8. Area specific resistance (ASR) of bare and spinel-coated 441 as a function of time. The measurements were carried out in air at 800 °C with a constant applied current of 500 mA cm^{-2}. $La_{0.8}Sr_{0.2}MnO_3$ paste was used as the contact material.

was higher than that of the bare sample at the beginning of the measurement, but which decreased over time and finally stabilized at about 4 mΩ cm^2. While the ASR of the bare 441 was primarily attributable to the scale growth, the contact resistance of the coated sample might have been dependent on several factors, including scale growth beneath the protection layer (tending to increase ASR) and improvement in the electrical contact at the contact material/coating interface due to interactions between the LSM contact material and the spinel (which might tend to decrease ASR). The observed diffusion of Fe from the alloy into the spinel may also have affected the conductivity of the spinel coating.

Fig. 10(a) shows the SEM cross-section analysis of the bare 441 and LSM contact material after the electrical measurement. A uniform scale was grown on the 441 substrate, which appeared to have reacted with the LSM contact material at their interface to form a dense interfacial layer. EDS point analysis confirmed the second phases in the surface region of the steel to be rich in Nb and Si. The line scan indicated that the scale was rich in Mn in the outer layer and rich in Cr in the sub-layer, confirming a dual layer structure with $(Mn,Cr)_3O_4$ spinel-rich top layer and chromia or chromia-rich sub-layer. Importantly, there was no Si enrichment or silica layer formation at the scale/metal interface, in spite of the relatively high residual Si content (0.47%) in the steel. This is due to the ability of Nb to capture the Si, forming the observed Laves phase precipitates that reduced Si activity in the steel substrate and thus inhibited the formation of an insulating silica layer at the metal/scale interface. The low ASR of 441, especially in the early stages of oxidation, further demonstrated the lack of silica layer formation at the interface. While there was evidence of Cr migration into the LSM contact material from the scale grown on the bare 441, no evidence of Cr-migration through the coating or into the LSM contact materials was observed for the coated sample, although, as noted previously, some Fe diffusion into the spinel coating was indicated. Combined with the aforementioned X-ray diffraction analysis, it is clear that, during the high temperature heat treatment, the spinel, with an initial bulk composition of $Mn_{1.5}Co_{1.5}O_4$ and a cubic-and tetragonal-mixed structure at room temperature, evolved into a $(Mn,Co,Fe)_3O_4$ spinel which retained its high temperature cubic structure when cooled to room temperature. Similar to the bare 441 sample, there was no formation of an insulating silica layer at the scale/metal interface, as indicated by the flat Si EDS profile across the interface. The lack of silica layer formation was further confirmed on additional bare and coated

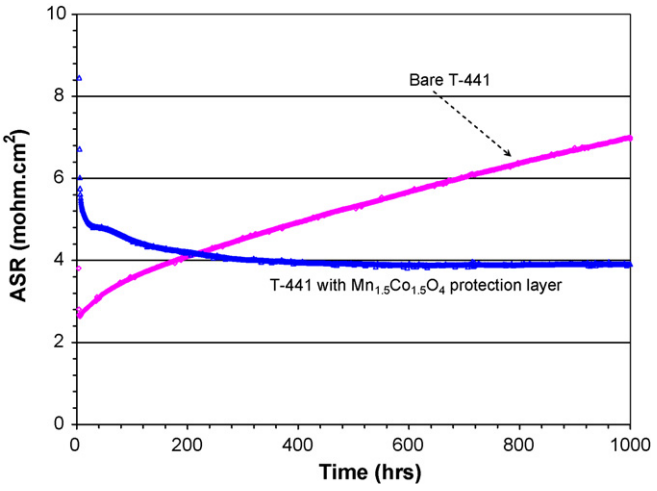

Fig. 9. Area specific resistance of bare and spinel-coated 441 as a function of time. The measurements were carried out in air at 750 °C with a constant applied current of 500 mA cm^{-2}. $La_{0.8}Sr_{0.2}MnO_3$ paste was used as the contact material.

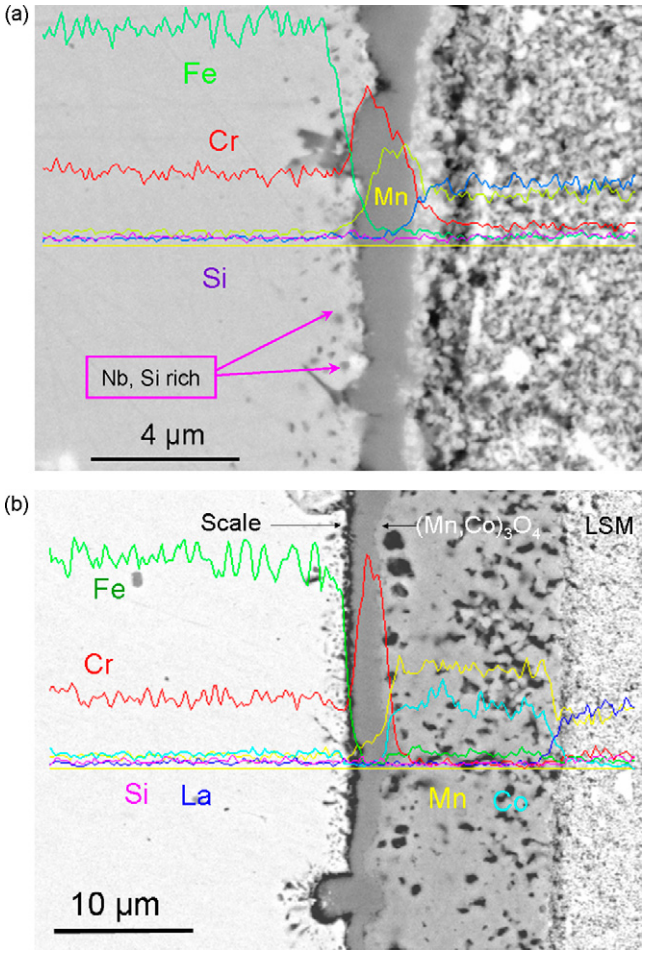

Fig. 10. SEM cross-section, along with EDS line scan, of 441: (a) bare alloy after electrical evaluation at 800 °C in air for 500 h and (b) spinel-coated alloy after 1000 h of electrical evaluation. $La_{0.8}Sr_{0.2}O_3$ paste was used as the contact material for the tests.

samples. While the lack of silica layer formation is encouraging, there are concerns regarding delamination that was observed along the scale/metal interfaces. Although it is likely that the delamination occurred during sample polishing, its presence may indicate that the scale/metal interface will be the "weak link" that limits the bonding strength and structural stability of spinel-coated 441.

In addition to the short-term tests, longer ASR tests were also carried out on bare and coated 441. As shown in Fig. 11, the ASR of bare 441 increased to about 60 mΩ cm^2 after nearly 6000 h of oxidation in air at 800 °C. In contrast, the spinel-coated sample exhibited stable ASR of around 12 mΩ cm^2 during the long-term testing. It is noted that the tests were interrupted twice by unscheduled power break-down at around 650 and 2800 h, respectively. The unscheduled thermal event caused a discontinuous increase in the ASR of bare 441, indicating contact problem or likely a detachment of the scale from the metal substrate. In contrast, the ASR of the coated sample returned to the previous level, indicating that application of the spinel protection layers helped improve the surface stability of the Fe–Cr–Nb–Ti stainless steel.

Overall it appears that the bare 441 represents a promising alloy chemistry that inhibits the formation of an insulating silicon layer at the alloy/scale interface. This indicates the feasibility of using alloy chemistry modifications to develop cost-effective SOFC inter-

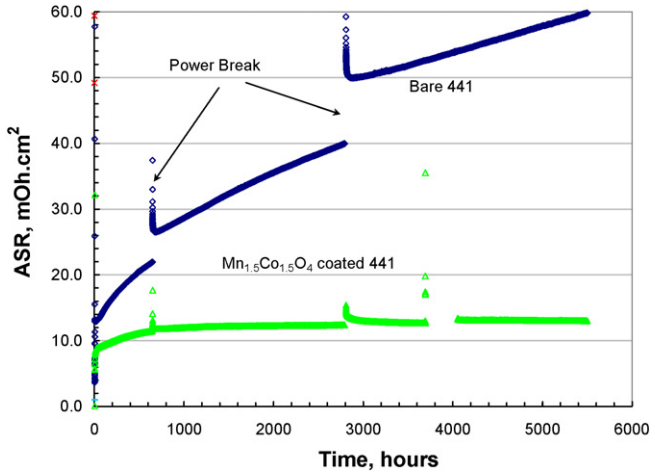

Fig. 11. Long-term area specific resistance (ASR) of bare and spinel-coated 441 as a function of time. The measurements were carried out in air at 800 °C with a constant applied current of 500 mA cm^{-2}. $La_{0.8}Sr_{0.2}MnO_3$ paste was used as the contact material.

connects based on ferritic stainless steels. However, for long-term stability and prevention of Cr-migration from the steel substrate, protective coatings are still needed.

4. Conclusions

Investigations into the metallurgy, oxidation behavior, and electrical performance indicate a promising alloy chemistry in 441 ferritic stainless steel for SOFC interconnect applications. Minor alloying additions of Nb (and Ti) led to Laves phase formation both inside grains and along grain boundaries during exposure in the intermediate SOFC operating temperature range. The Laves phase which precipitated along grain boundaries was rich in Si. The capture of Si in the Laves phase prevented formation of an insulating silica layer at the scale/metal interface. Because of this, 441 demonstrated low ASR during the early stages of oxidation. However, the substantial increase in ASR due to oxide scale growth over time demonstrated the need for a conductive protection layer. In particular, $Mn_{1.5}Co_{1.5}O_4$ coatings drastically improved the electrical performance of the ferritic stainless steel 441. The spinel coatings appeared to limit oxygen inward diffusion, which thus reduced the scale growth rate beneath the coatings. While some diffusion of Fe into the coatings was observed, the coatings blocked Cr outward migration and thus would be expected to prevent potential Cr-poisoning of SOFC cathodes.

Acknowledgements

The authors would like to thank Jim Rakowski at Allegheny Techologies, Inc. for providing the alloy samples, and Nat Saenz, Shelly Carlson, and Jim Coleman at PNNL for their assistance in metallographic and SEM sample preparation and analysis. The authors would also like to acknowledge helpful discussions with Wayne Surdoval, Ayyakkannu Manivannan, and Briggs White at the National Energy Technology Laboratory (NETL). The work summarized in this paper was funded by the U.S. Department of Energy's Solid-State Energy Conversion Alliance (SECA) Core Technology Program. PNNL is operated by Battelle Memorial Institute for the U.S. Department of Energy under Contract DE-AC06-76RLO 1830.

References

[1] W.J. Quaddakkers, J. Piron-Abellan, V. Shemet, L. Singheiser, Mater. High Temp. 20 (2003) 115.
[2] J.W. Fergus, Mater. Sci. Eng. A 397 (2005) 271.
[3] Z.G. Yang, K.S. Weil, D.M. Paxton, J.W. Stevenson, J. Electrochem. Soc. 150 (2003) A1188.
[4] W.Z. Zhu, S.C. Deevi, Mater. Sci. Eng. A 348 (2003) 227.
[5] Z.G. Yang, Inter. Mater. Rev. 53 (2008) 39–54.
[6] D. Dulieu, J. Cotton, H. Greiner, K. Honegger, A. Scholten, T. Seguelong, in: P. Stevens (Ed.), Proceedings of Third European SOFC Forum, European Solid Oxide Fuel Cell Forum, Switzerland, 1998, p. 447.
[7] T. Horita, H. Kishimoto, K. Yamaji, Y. Xiong, N. Sakai, M.E. Brito, H. Yokokawa, J. Power Sources 176 (2008) 54.
[8] W.J. Quadakkers, V. Shemet, L. Singheiser, US Paten No. 2,003,059,335 (2003).
[9] J.P. Abeilan, V. Shemet, F. Tietz, L. Singheiser, W.J. Quadakkers, in: S.C. Singhal, M. Dokiya (Eds.), Proceedings of the Seventh International Symposium on Solid Oxide Fuel Cells The Electrochemical Proceedings Series, Pennington, NJ, PV2001-16, 2001, p. 811.
[10] Z.G. Yang, J.S. Hardy, M.S. Walker, G. Xia, S.P. Simner, J.W. Stevenson, J. Electrochem. Soc. 151 (2004) A1825.
[11] T. Uehara, A. Toji, T. Ohno, in: M. Mogensen (Ed.), Proceedings of Sixth European SOFC Forum, European Solid Oxide Fuel Cell Forum, Switzerland, 2004, p. 1654.
[12] T. Horita, Y. Xiong, K. Yamaji, N. Sakai, H. Yokokawa, J. Electrochem. Soc. 150 (2003) A243.
[13] M. Schuisky, A. Rosberg, L. Mikkelson, P. Hendriksen, N. Christiansen, J. Gutzon Larsen, Fuel Cell Seminar, Courtesy Associates, Washington, DC, 2007.
[14] J. Froitzheim, G.H. Meier, L. Niewolak, P.J. Ennis, H. Hattendorf, L. Singheiser, W.J. Quadakkers, J. Power Sources 178 (2008) 163.
[15] S. Chandra-Ambhorn, Y. Wouters, L. Antoni, F. Toscan, A. Galerie, J. Power Sources 171 (2007) 688.
[16] Z.G. Yang, G. Xia, J.W. Stevenson, Electrochem. Solid State Lett. 8 (2005) A168.
[17] X. Chen, P.Y. Hou, C.P. Jacobson, S.J. Visco, L.C. De Jonghe, Solid State Ionics 176 (2005) 425.
[18] M. Zahid, F. Tietz, D. Sebold, H.P. Buchkremer, in: M. Mogensen (Ed.), Proceedings of Sixth European SOFC Forum, European Solid Oxide Fuel Cell Forum, Switzerland, 2004, p. 820.
[19] Z.G. Yang, G.-G. Xia, G.D. Maupin, J.W. Stevenson, Surf. Coat. Technol. 201 (2006) 4476.
[20] Z.G. Yang, G.-G. Xia, S.P. Simner, J.W. Stevenson, J. Electrochem. Soc. 152 (2005) A1896.
[21] V.I. Gorokhovsky, P.E. Gannon, M.C. Deibert, R.J. Smith, A. Kayani, M. Kopczyk, D. VanVorous, Z. Yang, J.W. Stevenson, S. Visco, C. Jacobson, H. Kurokawa, S.W. Sofiee, J. Electrochem. Soc. 153 (2005) A1886.
[22] X. Deng, P. Wei, M. Reza Bateni, A. Petric, J. Power Sources 160 (2006) 1225.
[23] R.J. Hodges, Corrosion 27 (1967) 164.
[24] A.P. Bond, Trans. AIME 245 (1969) 2127.
[25] N. Fujita, H.K.D.H. Bhadeshia, M. Kikuchi, Mater. Sci. Eng. 12 (2004) 273.
[26] Stainless Steels AL 441HP^{TM} Alloy, Technical Report, ATI Allegheny Ludlum Corp., 2005.
[27] J.-C. Zhao, M.R. Jackson, L.A. Peluso, Acta Mater. 51 (2003) 6395.
[28] M.E. Schlesinger, H. Okamoto, A.B. Gokhale, R.J. Abbaschian, J. Phase Equilib. 14 (1993) 502.
[29] B.P. Bewlay, M.R. Jackson, R.R. Bishop, J. Phase Equilib. 19 (1998) 577.
[30] N. Fujita, K. Ohmura, A. Yamamoto, Mater. Sci. Eng. A351 (2003) 272.
[31] N. Fujita, K. Ohmura, M. Kikuchi, T. Suzuki, S. Funaki, I. Hiroshige, Scripta Mater. 35 (1996) 705.
[32] J. Mougin, M. Dupeux, L. Antoni, A. Galerie, Mater. Sci. Eng. A359 (2003) 44.
[33] C. Gleitzer, Mater. Res. Bull. 15 (1980) 507.
[34] High Tempearture Alloy Crofer22 APU, Materials Data Sheet No. 4046, ThyssenKrupp VDM, 2005.